energies

MDPI

Article

Influence of Train Speed on Transient Current Evolution in Traction Network Under Pantograph–Catenary Offline Conditions

Changchun Lv [1,2], Wanting Xue [3], Jun Guo [3,*] and Xuan Wu [1]

[1] Beijing Institute of Astronautic System Engineering, Beijing 100076, China; lvchchpaper@163.com (C.L.); wuanwupaper@163.com (X.W.)
[2] School of Electronics and Information Engineering, Beihang University, Beijing 100191, China
[3] School of Electrical Engineering, Xi'an Jiaotong University, Xi'an 710049, China; xwting@stu.xjtu.edu.cn
* Correspondence: junguo@mail.xjtu.edu.cn

Abstract

To investigate the influence of train operating speed on the transient characteristics of the pantograph–catenary arc, this paper establishes an integrated simulation model encompassing the traction network, electric locomotive, and arc. In this model, the traction network adopts a chain circuit model based on multi-conductor transmission line theory. The electric locomotive model considers the train body and the on-board transformer. For the pantograph–catenary offline arc, an improved Habedank model is employed, which takes the train operating speed and arc current as variables. Based on this model, this paper systematically investigates the variation patterns of arc electrical parameters and transient currents in each line of the traction network with train operating speed under pantograph–catenary offline. The simulation results indicate that as train speed increases, both the steady-state arc voltage and the maximum voltage at arc ignition rise, and the arc extinction time at current zero-crossing is prolonged. The peak arc currents on the contact wire, feeder, protective wire, and rails decrease, while the transient current on the ground wire increases. This study can provide a reference for the electromagnetic compatibility design, insulation coordination optimization, and electromagnetic protection of high-speed railway traction power supply systems.

Keywords: pantograph–catenary offline; traction network; arc characteristics; high-speed railway; electromagnetic compatibility

Check for updates

Academic Editor: Giovanni Lutzemberger

Received: 26 February 2026
Revised: 10 April 2026
Accepted: 12 April 2026
Published: 15 April 2026

Copyright: © 2026 by the authors. Licensee MDPI, Basel, Switzerland. This article is an open access article distributed under the terms and conditions of the Creative Commons Attribution (CC BY) license.

1. Introduction

The traction power supply system of electric railway provides continuous electrical energy to trains through the sliding contact between the pantograph and the catenary [1]. The quality of pantograph–catenary current collection directly determines the reliability and safety of train operation [2]. With the rapid development of electrified railways, train operating speeds have been continuously increasing [3], leading to intensified dynamic interactions between the pantograph and the contact wire [4], and pantograph–catenary disconnection phenomena occur frequently. At the moment of pantograph–catenary separation, the air within the gap is broken down by the voltage of the contact wire, forming a high-temperature plasma arc [5]. The substantial energy contained within the arc not only ablates key components such as the contact wire and pantograph strip [6], seriously threatening the service life of the pantograph–catenary system, but also triggers intense transient

electromagnetic processes. The resulting overvoltage and overcurrent propagate along the traction network conductors, affecting the train and the electromagnetic environment around it [7].

To deeply understand and effectively mitigate the hazards of pantograph–catenary arcs, scholars globally have investigated the characteristics of pantograph–catenary offline arcs from the perspective of multiple influencing factors. In terms of experimental measurement, Niu et al. [8] investigated the offline arc radio frequency and in-train low-frequency electromagnetic exposure of high-speed railway trains on the Wuhan-Guangzhou line. By combining a field test with a semi-physical simulation test, the study found that the pantograph–catenary offline arc exhibits the richest frequency spectrum within the 30–300 MHz range. Yang et al. [9] developed a railway megawatt-level pantograph–catenary offline arc electromagnetic disturbance test platform based on supercapacitor energy storage. Using this platform, experiments were conducted on the electromagnetic disturbance characteristics of fixed-gap breakdown arcs in the pantograph–catenary system, and the corresponding relationship between the pulse current in the circuit and the electromagnetic radiation was analyzed. By establishing a pantograph–catenary offline arc simulation experiment system, Wu et al. [10] captured the arc morphology using a high-speed camera and analyzed the dynamic evolution process of the arc ignition and the influence of arc current on the arc morphology characteristics. In terms of simulation, Zou et al. [11] employed the Mayr and Schwarz models to analyze the voltage waveform, conductivity, and power curve of the pantograph–catenary arc at elevations exceeding 4000 m in electrified railways. This analysis determined the influence of altitude on the electrical characteristics of the pantograph–catenary arc. Xu et al. [12] established a magnetohydrodynamic model of the pantograph–catenary arc to obtain the internal temperature distribution characteristics of the arc. Through this model, the authors summarized the effects of different air pressures and airflow velocities on the temperature and voltage of the pantograph–catenary arc. Ma et al. [13] developed a physical analysis model for the steady-state combustion of a pantograph–catenary arc based on fluid dynamics theory. Using this model, the influence of different contact wire profile radii and strip material thermal conductivities on the extent of the high-temperature region on the contact wire and strip surface was determined. These findings provide a reference for reducing electrical wear in the pantograph–catenary system.

Specifically, the pantograph–catenary offline arc does not occur at a fixed location but slides along the contact wire as the train continuously moves forward [14], with its roots sliding along the contact wire [15] and the arc channel being continuously stretched. This dynamic stretching process causes the radius of the arc column to gradually contract and the arc channel length to increase continuously, leading to distortion of the arc's voltage-current characteristic [16]. At the same time, the strong airflow generated by the high-speed movement of the train exerts a significant blowing effect on the arc plasma [17]. This accelerates the diffusion and recombination of charged particles, significantly enhancing the dielectric recovery strength [18], which makes the arc more likely to extinguish when the current passes through zero. It can be seen that the train operating speed not only directly affects the electrical parameters of the arc by altering its geometric morphology [19], but also indirectly influences the arc duration and energy injection process by modifying the heat dissipation conditions and arc-extinguishing environment [20]. Finally, the train operating speed affects the overvoltage and overcurrent caused by pantograph–catenary disconnection, as well as the distribution and spectral characteristics of the excited spatial electromagnetic field [21].

Currently, researchers from multiple countries have extensively studied the influence of train operating speed on pantograph–catenary arcs. Chen et al. [17] developed a dy-

namic model of the pantograph–catenary arc based on the theories of transverse blowing arc, longitudinal blowing arc, and energy balance. The model was used to investigate the influence of the high-speed airflow field on the arc dissipation power. The results indicate that the arc dissipation power increases with train speed. Zhang et al. [22] conducted field measurements of pantograph–catenary offline arcing at the steady arm points of high-speed railway catenaries. Based on a pantograph–catenary transient dynamics simulation model, the influences of train speed, contact wire tension, and steady arm mass on pantograph–catenary offline duration were investigated. Ma et al. [23] established a pantograph–catenary arc discharge model by comprehensively considering the relationships between train speed and the pantograph–catenary offline probability, contact force, and dynamic uplift of the contact wire. Based on this model, the trends in the frequency and magnitude of electromagnetic disturbances caused by pantograph–catenary offline arc discharges at different train operating speeds were analyzed. Pan et al. [24] investigated the electrical characteristics and influencing factors of the pantograph–catenary arc when a high-speed train passes through an articulated split-zone insulator. The results indicated that the faster the train speed, the faster the arc extinguishes.

Existing studies have made valuable contributions by investigating the electromagnetic interference characteristics of pantograph–catenary arcs and by analyzing the influence of train speed on arc morphology, temperature, duration, and other electrical properties. However, these studies often simplify the traction network and neglect the electromagnetic coupling among multiple conductors, such as the contact wire, protective wire, ground wire, and rail. As a result, they are unable to precisely quantify how train speed affects the distribution of transient energy across the different current paths within the traction network.

To address these gaps, this paper constructs an integrated simulation model that combines two key components. First, the traction network is represented as a chain circuit based on multi-conductor transmission line theory. This representation accurately describes the distributed parameters and the electromagnetic coupling relationships among the contact wire, positive feeder, protective wire, ground wire, and rail. Second, an improved Habedank dynamic arc model is adopted to characterize the nonlinear time-varying behavior of the pantograph–catenary arc. Unlike the conventional Habedank model, which assumes constant arc parameters, the improved version replaces the total dissipation power constant and the arc voltage constant with speed-dependent expressions derived from experimentally validated relationships in the literature. This allows the model to capture the influence of train speed on arc dynamics. By integrating these two components, the proposed model enables, for the first time, a quantitative analysis of how transient current is distributed across the multiple conductors of the traction network under varying train speeds. This study systematically analyzes the evolution of arc characteristics and the transient current distribution within the multi-conductor traction network during pantograph–catenary offline condition under different train speeds. The primary contribution lies in quantitatively revealing how train speed governs the allocation of transient energy across multiple conductors, a mechanism that has not been explicitly clarified in prior work. These results offer a theoretical foundation for the optimization of traction network design and the evaluation of electromagnetic compatibility risks in high-speed railways.

2. Modeling

This section establishes a comprehensive simulation model covering the traction network, electric locomotives, and pantograph–catenary arc. The traction network employs a chain circuit model based on multi-conductor transmission line theory. The electric locomotive model considers the train body and the on-board transformer. The

pantograph–catenary arc utilizes an improved Habedank model with the train operating speed and arc current as variables.

2.1. Power Supply System of Electric Traction

The electrified railway traction power supply system serves as the core infrastructure for providing power to electric locomotives [25]. Its function is to convert the three-phase electrical energy from the power system into single-phase alternating current suitable for locomotives and deliver it via the traction network [26]. This system generally employs a single-phase AC system with a power frequency and a rated voltage of 27.5 kV [27]. Under the all-parallel autotransformer feeding mode, the traction network mainly consists of the contact wire (C), carrier cable (J), positive feeder (F), rail (RW), protective wire (P), and ground wire (G). A typical spatial arrangement is illustrated in Figure 1.

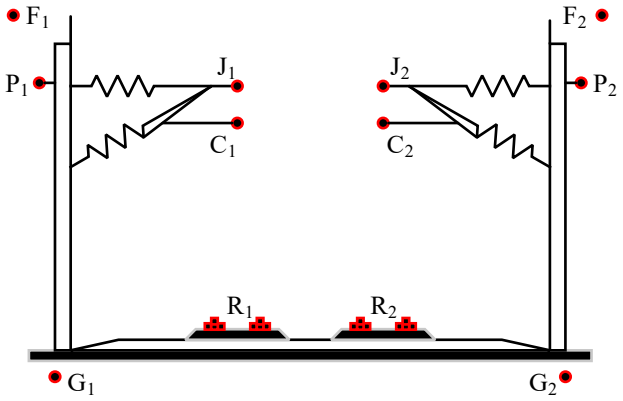


Figure 1. Spatial distribution map of the positions of conductors in the traction network with the fully parallel autotransformer power supply mode.

To accurately analyze the broad frequency-domain electromagnetic transient processes caused by pantograph–catenary offline arcs, this paper adopts a chain circuit model based on the multi-conductor transmission line theory [28] to model the traction network.

According to Carson's theory [29], combined with the specific parameters of the conductors, the unit-length self-impedance Z_{ii} of each conductor and the unit-length mutual impedance Z_{iq} between conductors are calculated as follows:

$$Z_{ii} = r_i + r_G + \mathrm{j}0.145\lg\frac{2.085}{R_{\varepsilon i}\sqrt{f\sigma \times 10^{-9}}}, \quad (1)$$

$$Z_{iq} = r_G + \mathrm{j}0.145\lg\frac{2.085}{d_{iq}\sqrt{f\sigma \times 10^{-9}}}, \quad (2)$$

where j is the imaginary unit, r_i is the equivalent resistance of any conductor I, r_G is the effective resistance of the equivalent ground return path, representing the electrical energy loss in the lossy ground, $R_{\varepsilon i}$ is the equivalent radius of any conductor i, d_{iq} is the distance between any conductors i and q, f is the current frequency, and σ is the ground conductivity.

Since the contact wire and the carrier cable are connected by droppers approximately every 10 m and are electrically similar, they can be merged into an equivalent overhead contact line conductor (T). Similarly, the left and right rails, being symmetrically positioned and electrically identical, can be equivalently merged into a single equivalent conductor (R), located at the center between the two rails.

The self-potential coefficient P_{ii} and mutual-potential coefficient P_{iq} of the overhead conductors are obtained using the image method. The relationship between a conductor and its image is illustrated in Figure 2.

$$P_{ii} = \frac{1}{2\pi\varepsilon_0} \ln\left(\frac{2h_{ig}}{r_i}\right), \tag{3}$$

$$P_{iq} = \frac{1}{2\pi\varepsilon_0} \ln\left(\frac{D_{iq}}{d_{iq}}\right), \tag{4}$$

where ε_0 is the vacuum permittivity, h_{ig} represents the straight-line distance from any conductor i to the ground, and D_{iq} is the distance between conductor i and the image of conductor q.

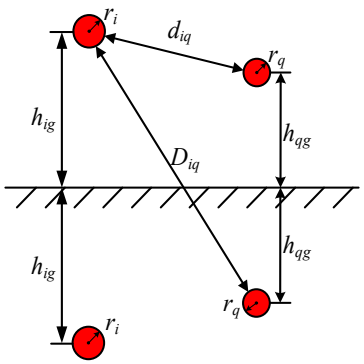


Figure 2. Schematic diagram of the conductor and its image.

The distributed capacitance coefficient matrix **C** is the inverse of the potential coefficient matrix **P**. Based on the electrical parameter values of each conductor's self-impedance, self-capacitance, mutual impedance, and mutual capacitance calculated as described above, a per-unit-length τ-type equivalent circuit model of the traction network is established, as shown in Figure 3.

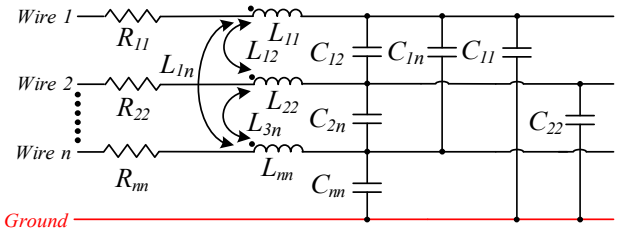


Figure 3. Equivalent model of the traction network per unit length.

The τ-type equivalent circuits are connected in a chain, where the length of the total segment corresponds to the actual line length. Other electrical equipment can be treated as series or parallel components distributed along the line. Ultimately, a chain circuit model is constructed that accurately reflects the spatial structure and electromagnetic coupling relationships of the traction network, as shown in Figure 4.

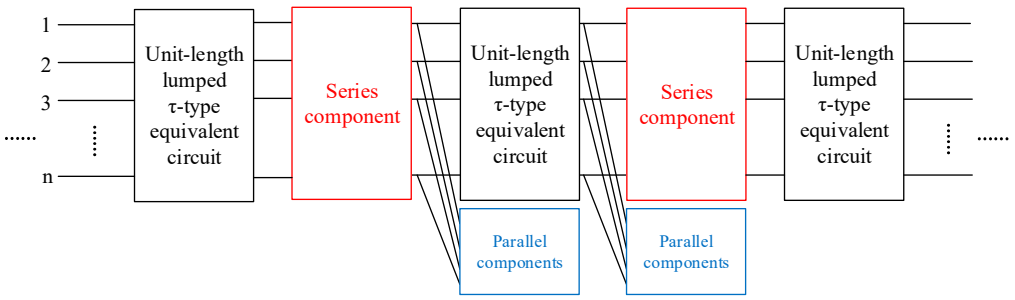


Figure 4. Traction chain circuit model diagram.

2.2. Electric Locomotive

In this paper, the train is configured with one motor car and two trailer cars, where the locomotive head is the motor car. A traction transformer and other equipment are installed beneath this motor car to provide traction power for the train.

The equivalent impedance of the transformer secondary side under normal operation is calculated using the following formula based on the equivalent load when the transformer operates at its rated power:

$$R_T = \frac{U_{2N}^2}{S_N/2}, \tag{5}$$

where U_{2N} is the rated voltage of the secondary side of the traction transformer, and S_N is the rated power of the traction transformer.

According to Equation (5), the transformer can be represented by an equivalent impedance, as shown in Equation (6):

$$R_T{}' = \left(\frac{n_1}{n_2}\right)^2 \frac{R_T}{2}, \tag{6}$$

where n_1 and n_2 are the number of turns of the primary winding and secondary winding of the transformer, respectively.

Accordingly, the train-equivalent circuit is constructed as shown in Figure 5. This equivalent model includes the equivalent resistance Z_L of the motor car, the equivalent resistance Z_C of the trailer car, the equivalent resistance $R_T{}'$ of the transformer, the combined equivalent resistance R_J of the four grounding carbon brushes for a single car, the equivalent resistance R_L of the grounding resistor, and the inter-car connection resistance R_C.

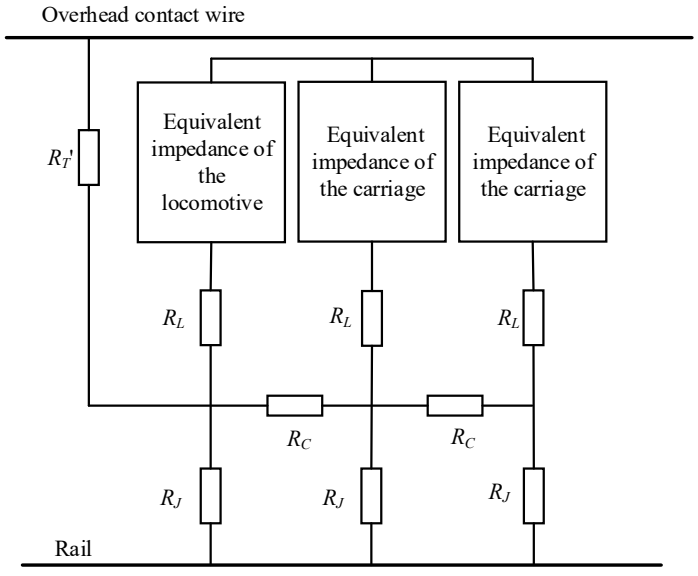


Figure 5. Equivalent circuit diagram of the train.

The locomotive model described above is established based on the equivalent impedance at the fundamental frequency. However, the present study involves higher frequency components associated with pantograph–catenary arc transients, where the frequency range can extend up to several kilohertz. This frequency mismatch is acknowledged as a limitation of the simplified model. To address this limitation, we have explicitly examined how variations in the locomotive impedance affect the conductor currents of the traction network during arc events. A sensitivity analysis was performed by varying the locomotive equivalent inductance independently within a reasonable range. Specifically, the inductance was varied by ±50%. The results show that under this variation, the peak

currents on all conductors also change by less than 1×10^{-6}% relative to the baseline case using the fundamental frequency model. The primary reason is that during the arc transient, the current distribution among conductors is dominated by the line-distributed parameters rather than by the local impedance at the locomotive. Therefore, even if the locomotive impedance varies within a certain range, the core conclusions regarding current distribution trends of this paper remain valid.

2.3. Pantograph–Catenary Arc

The pantograph–catenary arc is inherently a strongly nonlinear, time-varying physical discharge process. To model the equivalent resistance of the arc, the academic community has successively proposed the Cassie model and the Mayr model based on energy balance. These two models describe the characteristics of the arc column and the arc root, respectively, but both have limitations in their applicability [30]. Specifically, the Cassie model is suitable for high-current, high-temperature arcs where the arc conductance varies rapidly, while the Mayr model is more appropriate for low-current conditions near current zero-crossing. Given that pantograph–catenary offline arcs often involve wide-range current variations and exhibit both column and root characteristics, the use of a single model would inevitably introduce limitations in capturing the full dynamic behavior. To address this, Habedank et al. connected them in series, forming a composite model that can more comprehensively reflect the dynamic characteristics of the arc [31].

This study focuses on the influence of the pantograph–catenary disconnection arc on the current distribution in the traction network. The Habedank model is adopted because it simultaneously accounts for the physical processes of both the arc column and the arc root. This enables a more accurate representation of the arc's time-varying resistance under actual operating conditions. This combined approach helps ensure the reliability of the traction network current distribution analysis under arcing scenarios. However, the Habedank model assumes the arc voltage E_{arc} and the arc power loss P_{loss} to be constants E_0 and P_0, respectively. During the actual pantograph–catenary offline process, the offline distance varies continuously due to the influence of train speed; therefore, E_{arc} and P_{loss} are not constant. Consequently, the Habedank arc model needs to be modified to accurately represent the actual conditions of train pantograph–catenary offline arcs.

As a plasma column with an extremely high temperature, the arc releases a substantial amount of heat into the surrounding air. When the train operates at high speed, the air around it flows rapidly. This airflow passes over the high-temperature arc, carrying away its heat, thereby cooling the arc and suppressing its development and maintenance. Generally, the strong airflow generated by a high-speed train, which flows parallel to the roof surface, can be decomposed into two components relative to the arc [17]: one is the longitudinal blowing airflow, which is parallel to the arc direction, and the other is the transverse blowing airflow, which is perpendicular to the arc direction, as shown in Figure 6.

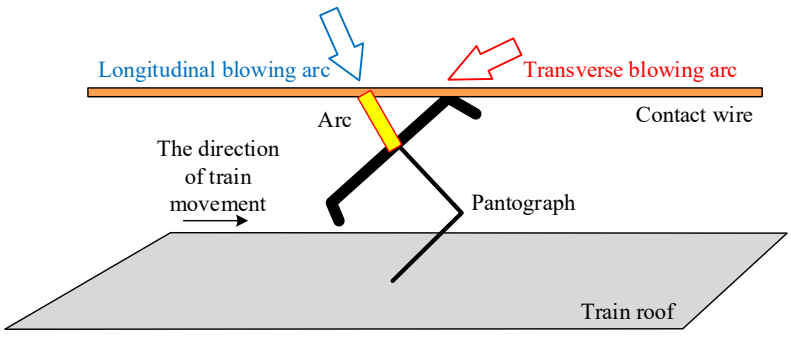


Figure 6. Schematic diagram of airflow blowing directions relative to the arc.

During train operation, temporary separation between the pantograph and catenary often occurs due to factors such as mechanical vibration or irregularities in the contact wire, leading to an offline arc. As this offline gap is generally small, it can be assumed that the resulting arc is approximately perpendicular to the train roof plane. Therefore, the arc length L is approximately equal to the distance r_{pc} between the pantograph and the catenary. Under these conditions, only the part of the convective cooling power contributed by the transverse blowing effect remains, while the convective effects in other directions can be neglected. According to Ref. [32], the convective power of pantograph–catenary arc P_k and the distance r_{pc} between the pantograph and the catenary can be obtained by:

$$P_k = 0.1892\sqrt{i_{arc}}(v + 36) \cdot L, \tag{7}$$

$$r_{pc} = 4.571 \times 10^{-5}v^2 + 0.238v - 1.411, \tag{8}$$

where i_{arc} is the arc current, and v is the train operating speed.

The total dissipated power P_{loss} and the arc voltage E_{arc} of the pantograph–catenary offline arc can be calculated as:

$$P_{loss} = \frac{P_k}{80\%} = \sqrt{i_{arc}}(1.08 \times 10^{-5}v^3 + 0.06v^2 + 1.69v - 12.01), \tag{9}$$

$$E_{arc} = 15L = 6.86 \times 10^{-4}v^2 + 3.57v - 21.17, \tag{10}$$

To accurately simulate the impact of pantograph–catenary offline arcs on the traction power supply system at different train speeds, the dissipation power constant and arc voltage constant in the classical Habedank arc model are replaced by the expressions related to the train operating speed, as given in Equations (9) and (10). This yields the modified Habedank arc model as shown in Equation (11):

$$\begin{cases} \frac{dg_C}{dt} = \frac{1}{\tau_0 g^\alpha}\left[\frac{{i_{arc}}^2}{\left(6.86\times10^{-4}v^2+3.57v-21.17\right)^2 g_C} - g_C\right] \\ \frac{dg_M}{dt} = \frac{1}{\tau_0 g^\alpha}\left[\frac{{i_{arc}}^2}{\sqrt{i_{arc}}(1.08\times10^{-5}V^3+0.06v^2+1.69v-12.01)} - g_M\right], \\ \frac{1}{g} = \frac{1}{g_C} + \frac{1}{g_M}, \end{cases} \tag{11}$$

where τ_0 is the initial time constant of the arc, α is a constant, g_C is the conductance of the Cassie model, τ_C is the time constant of the Cassie model, g_M is the conductance of the Mayr model, τ_M is the time constant of the Mayr model, and g is the arc conductance.

To evaluate the robustness of the modified Habedank model and to quantify how the results depend on the coefficients, a sensitivity analysis is performed. Each of the seven coefficients is varied independently by ±50% while keeping all other parameters unchanged. The resulting variation in the peak transient current is shown in Table 1. The variation in the peak transient current is found to be within ±0.134% for all conductors. These very small changes indicate that the model outputs are not excessively sensitive to moderate perturbations in the coefficients.

Table 1. The variation in the peak transient current when the coefficient changes.

Coefficients		Variation in the Peak Transient Current (%)				
Before	**After**	**Contact Wire**	**Positive Feeder**	**Protective Wire**	**Ground Wire**	**Rail**
1.08×10^{-5}	1.62×10^{-5}	-1.61×10^{-5}	-1.08×10^{-5}	-1.69×10^{-6}	6.53×10^{-6}	-1.57×10^{-5}
	0.54×10^{-5}	1.62×10^{-5}	1.08×10^{-5}	1.71×10^{-6}	-6.09×10^{-6}	1.60×10^{-5}

Table 1. *Cont.*

Coefficients		Variation in the Peak Transient Current (%)				
Before	**After**	**Contact Wire**	**Positive Feeder**	**Protective Wire**	**Ground Wire**	**Rail**
0.06	0.09	-4.49×10^{-3}	-2.99×10^{-3}	-4.71×10^{-4}	1.72×10^{-3}	-4.39×10^{-3}
	0.03	4.49×10^{-3}	2.99×10^{-3}	4.71×10^{-4}	-1.72×10^{-3}	4.40×10^{-3}
1.69	2.535	-6.33×10^{-3}	-4.22×10^{-3}	-6.71×10^{-4}	2.41×10^{-3}	-6.20×10^{-3}
	0.845	6.33×10^{-3}	4.22×10^{-3}	6.72×10^{-4}	-2.41×10^{-3}	6.20×10^{-3}
−12.01	−18.015	2.25×10^{-3}	1.50×10^{-3}	2.38×10^{-4}	-8.50×10^{-4}	2.20×10^{-3}
	−6.005	-2.25×10^{-3}	-1.50×10^{-3}	-2.38×10^{-4}	8.50×10^{-4}	-2.20×10^{-3}
6.86×10^{-4}	10.29×10^{-4}	-5.15×10^{-4}	-2.67×10^{-4}	-5.32×10^{-5}	1.25×10^{-4}	-5.05×10^{-4}
	3.43×10^{-4}	5.15×10^{-4}	2.67×10^{-4}	5.32×10^{-5}	-1.25×10^{-4}	5.05×10^{-4}
3.57	5.355	-1.33×10^{-1}	-6.94×10^{-2}	-1.38×10^{-2}	3.25×10^{-2}	-1.31×10^{-1}
	1.785	1.34×10^{-1}	6.94×10^{-2}	1.38×10^{-2}	3.25×10^{-2}	1.31×10^{-1}
−21.17	−31.755	3.98×10^{-2}	2.06×10^{-2}	4.10×10^{-3}	-9.65×10^{-3}	3.89×10^{-2}
	−10.585	-3.97×10^{-2}	-2.06×10^{-2}	-4.10×10^{-3}	9.65×10^{-3}	-3.89×10^{-2}

3. Experimental Verification

During normal operation of the train, the pantograph–catenary offline arc is generated as the pantograph separates from the contact wire. Therefore, a pantograph-lowering arcing test can be used to simulate this process. To validate the correctness of the aforementioned model, this paper employs an equivalent testing platform for pantograph–catenary arcing, comprising components such as the pantograph, train, and catenary wire. The primary parameters of the test platform are shown in Table 2. The test train consists of two CR400BF electric locomotives. The load is connected to the low-voltage side of the transformer via the wheelsets and rail, and the load side of the pantograph is a 275 Ω equivalent resistance. This platform is capable of conducting pantograph–catenary offline discharge breakdown tests at a voltage of 27.5 kV and with a maximum breaking current of 100 A.

Table 2. Table of test platform parameters.

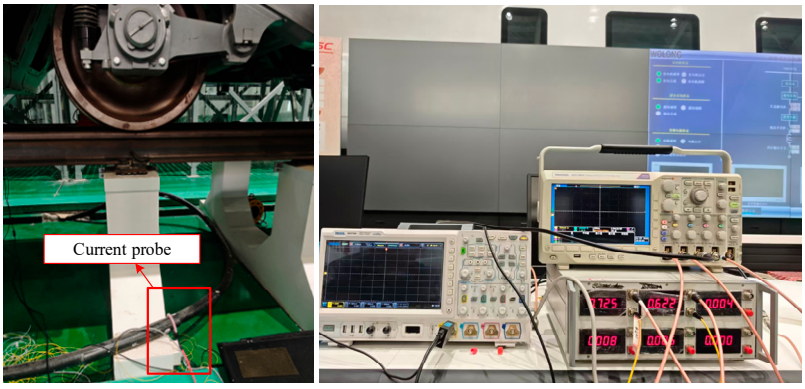
Equipment	Model	Specifications
Train	CR400BF	/
Contact wire	CTAH-120	/
Rail	P60	/
Equivalent load	/	Resistance: 275 Ω
Ground resistance	/	1 Ω

The authors of [32] indicate that the relationship between the arc length during pantograph–catenary disconnection and the train speed can be fitted as Equation (12). In the experiment, the final descent distances of the pantograph are selected as 3 mm, 28 mm and 48 mm, corresponding to the arc lengths at train operating speeds of 20 km/h, 120 km/h and 200 km/h, respectively. To ensure the validity and reliability of the collected data, multiple repeated tests are conducted for each pantograph descent distance.

$$L \approx 4.571 \times 10^{-5} v^2 + 0.238v - 1.411 \tag{12}$$

During the test, the contact wire remains stationary. In the initial state, the pantograph maintains stable contact with the contact wire. Subsequently, it is lowered by a motor drive

until it separates from the contact wire. At the moment when the pantograph actively detaches from the catenary under load, the distance between the contacts is extremely small but the voltage is extremely high. The air in the gap is ionized by electrons generated through field emission and thermionic emission, forming an arc. This arc maintains the original sinusoidal conduction state of the load current. The current in the circuit where the arc is present is measured using a CWTHF30B flexible current probe (Power Electronic Measurements Ltd., Nottingham, UK). The measurement position and receiving devices are shown in Figure 7.



(**a**) (**b**)

Figure 7. Measurement device and location diagram. (**a**) Current probe placement position; (**b**) signal receiving device.

The traction network in the test platform mainly consists of the contact wire and rails. Its spatial arrangement is illustrated in Figure 8, and the specifications and parameters of the wires are provided in Table 3. When calculating the impedance parameters of each conductor in the traction network, the two rails on the line are equivalently combined into a single equivalent conductor.

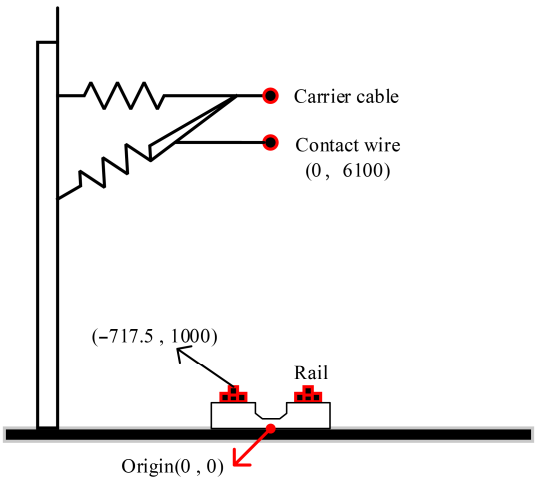


Figure 8. Schematic diagram of the traction network in the test platform.

Table 3. Wire specifications and parameters of the traction network.

Name	Model	Effective Resistance (Ω/km)	Equivalent Radius (mm)
Contact wire	CTAH-120	0.224	5.02
Rail	P60	0.135	12.79

Based on the modeling method described in Section 2, a simulation model for experimental verification is established. Using the results from the first test with a pantograph descent distance of 3 mm, the values of the equivalent inductance of the arc, as well as the ground capacitances of the catenary and the pantograph in the simulation model, are calibrated. The resulting simulation model is shown in Figure 9.

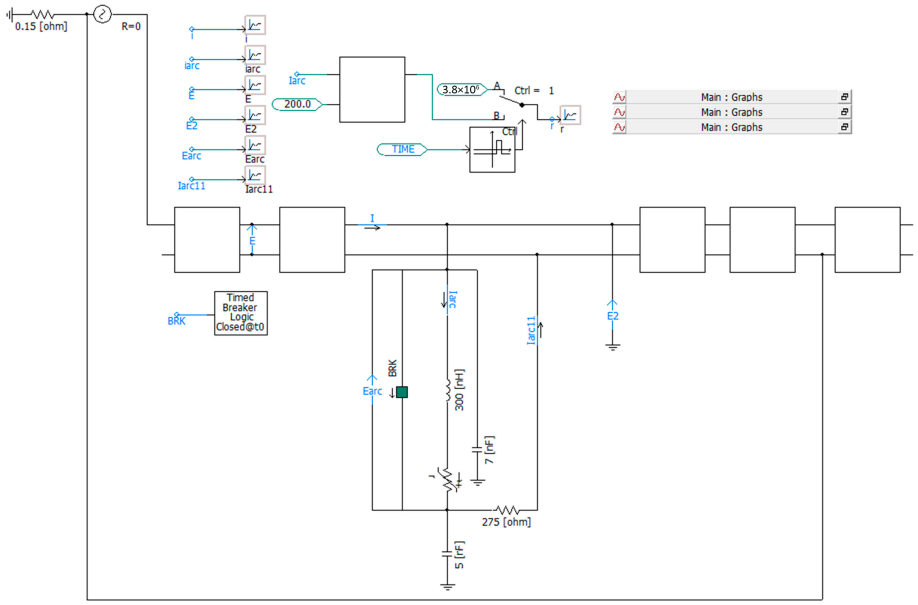


Figure 9. Simulation model of the test platform.

When the phase at the moment of arc initiation satisfies the conditions in Table 4, the measured and simulated waveforms of the load current under different gap distances are approximately consistent in both dominant frequency and amplitude, with an amplitude error of less than 1 dB.

Table 4. Comparison table of simulated and measured current amplitudes.

Speed (km/h)	Gap Distance (mm)	Measurement	Simulation		Error (dB)
		Current Amplitude (A)	Current Amplitude (A)	Phase (°)	
20	3	7.6	8.4	7.2	0.87
		9.8	9.7	8.3	0.09
		11.2	11.6	10.1	0.30
		12.1	12.3	10.9	0.14
		13.6	13.3	11.9	0.19
120	28	8.4	8.2	7.1	0.21
		11.2	11.7	10.2	0.38
		12.8	12.1	10.8	0.49
200	48	7.2	7.9	7.0	0.81
		10.1	9.8	8.2	0.26
		11.4	11.1	9.9	0.23

Taking the results of the first test as an example, the comparison between the simulated waveform and the measurement from the pantograph-lowering test is shown in Figure 10. The figures indicate that the simulated waveform is smoother than the measured waveform. This is because the simulation is based on an idealized mathematical model, which neglects factors present in the actual system such as minor disturbances, material inhomogeneities, and contact gaps. Additionally, the experimental waveform contains more high-frequency components, primarily due to environmental electromagnetic noise introduced during

the acquisition process and the background noise of the measurement equipment. These complex boundary conditions are typically simplified in the simulation. Overall, the waveforms obtained from the simulation and the experiment are in good agreement, and the spectrograms demonstrate a high degree of consistency in their main frequency components. This validates the accuracy and reasonableness of the established simulation model.

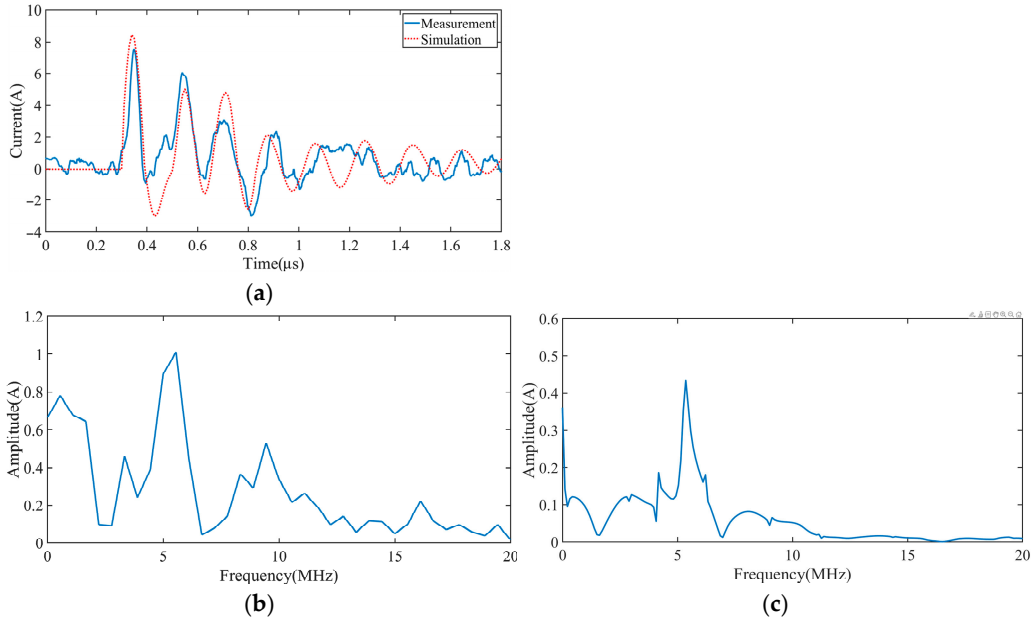


Figure 10. Comparison of measured and simulated waveforms. (**a**) Time domain; (**b**) frequency domain (measurement); (**c**) frequency domain (simulation).

4. Evolution of Transient Currents in the Traction Network

A simulation model is established using the parameters of the traction network (under the autotransformer supply system of electric traction) and the on-board transformer from an actual operating line. The wire specifications and parameters for each conductor in the traction power supply system used in this paper are presented in Table 5.

Table 5. Traction network wire specifications and parameters.

Name	Model	Effective Resistance (Ω/km)	Equivalent Radius (mm)
Contact wire	CTMH150	0.184	5.408
Carrier cable	JTMH120	0.242	5.306
Positive feeder	LBGLJ-240/30	0.114	9.372
Protective wire	LBGLJ-120/20	0.238	6.534
Ground wire	TJ-70	0.263	5.35
Rail	P60	0.135	12.79

The parameters of the traction substation transformer and the autotransformer are shown in Table 6. The traction substation is equivalently modeled using three-phase and three-winding transformers, while the autotransformers are equivalently modeled as two-winding transformers.

The parameters of the on-board traction transformer used in constructing the train-equivalent circuit are presented in Table 7.

Table 6. Table of traction power supply system equipment parameters.

Equipment	Parameter Name	Parameter Value
Traction substation transformer	Rated capacity Turns ratio	50 MVA 220 kV/27.5 kV/27.5 kV
Autotransformer	Rated capacity Turns ratio	25 MVA 27.5 kV/27.5 kV

Table 7. Table of on-board transformer parameters.

Winding	Primary Side	Secondary Side
Capacity (kVA)	3060	2570
Voltage (kV)	27.5	1.5
Frequency (Hz)	50	50
Efficiency	>95%	>95%

The train is placed as a parallel component at a distance of 3 km from the traction substation, with the arc model positioned between the catenary and the train model. A simulation model for the pantograph–catenary offline condition is established using PSCAD/EMTDC, as shown in Figure 11. When the phase of the catenary voltage at the moment of pantograph–catenary separation changes, the electromagnetic environment effects generated by the disconnection arc also vary accordingly. To investigate the most severe electromagnetic environment conditions, the phase at the moment of separation is set to $\Pi/2$.

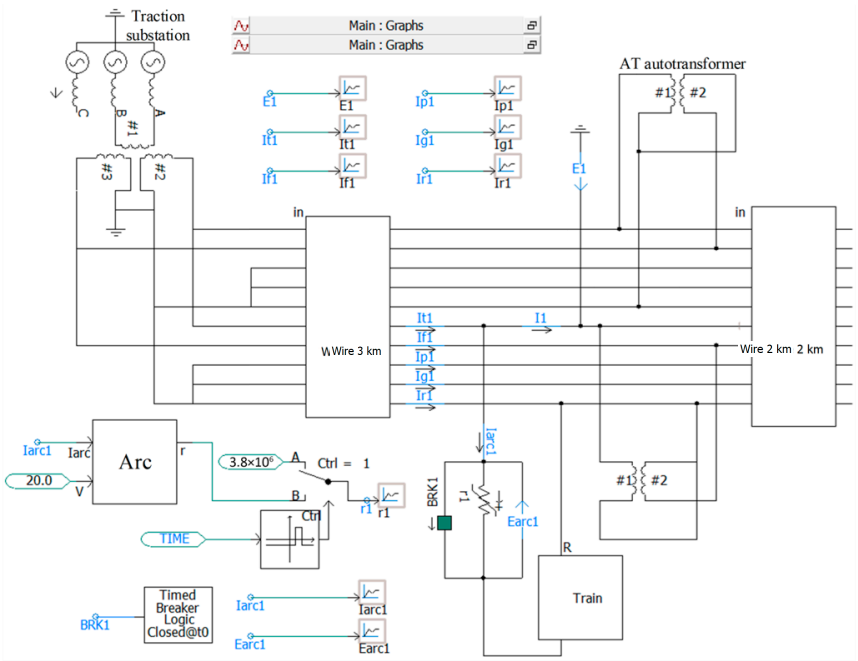
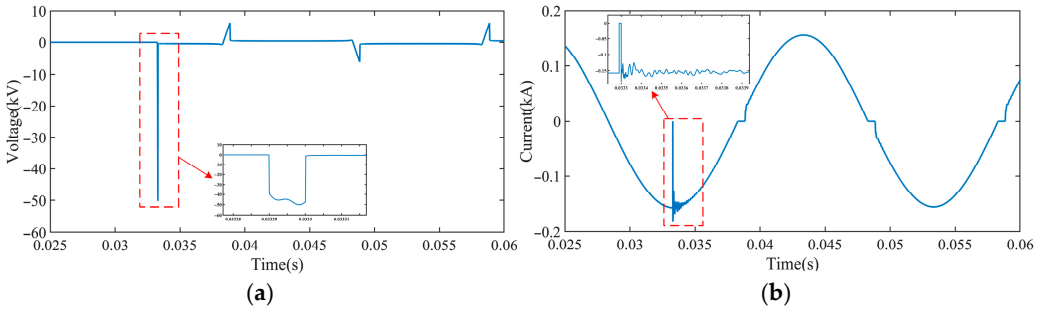


Figure 11. Simulation model diagram.

Taking the train operating speed of 100 km/h as an example, the arc voltage and current waveforms after the occurrence of pantograph–catenary disconnection are shown in Figure 12. It can be observed that at the instant of mechanical separation between the pantograph and the catenary, the arc current attempts to decrease sharply to zero. However, due to the significant inductance present in the circuit, the inductance generates a back electromotive force, causing the arc current to oscillate.



(**a**) (**b**)

Figure 12. Arc voltage and current waveform diagram. (**a**) Voltage; (**b**) current.

In the tiny gap at the moment of separation, the electric field strength becomes extremely high, leading to air breakdown and the formation of an arc plasma. At this instant, the arc voltage rapidly rises to the breakdown voltage of the air medium. As shown in Figure 12a, the arc voltage reaches its first peak. Once the arc is established, the arc voltage is maintained at a relatively stable lower value, and the arc current resumes its power frequency behavior. When the arc gap is stretched sufficiently large or when the current passes through zero, the arc extinguishes due to a lack of energy to sustain it; the arc voltage then quickly recovers to the system voltage, and the arc current drops to zero. Subsequently, the arc undergoes periodic cycles of ignition, combustion, extinction, and reignition with the current.

Taking the contact wire current at speeds of 20 km/h, 60 km/h, and 100 km/h as an example, the parameters related to the arc are shown in Table 8. When the traction current is the same, a higher train operating speed results in greater vibration amplitude upon pantograph–catenary separation. This leads to an increase in the arc gap length, consequently raising the voltage required for arc reignition. Therefore, the maximum voltage at arc ignition is higher, and the extinction time of the arc at current zero-crossing is also longer. Additionally, as the arc gap distance increases, the arc energy disperses more, requiring a higher voltage to sustain the arc. Consequently, the steady-state arc voltage is higher, and the transient oscillation peak of the arc current during reignition is also greater.

Table 8. Arc characteristics at zero-crossing current at different speeds.

Speed (km/h)	Maximum Arc-Starting Voltage (kV)	Stable Arc Voltage (kV)	Arc Extinction Time at Zero-Crossing Point of Current (s)
20	0.456	0.055	0
60	3.704	0.224	0.00032
100	6.189	0.414	0.00055

From an engineering perspective, as speed increases, the higher reignition peak current and longer arc duration accelerate material wear on both the contact wire and the pantograph strip. Therefore, high-speed lines should shorten the pantograph maintenance interval and enhance wear monitoring. The increase in arc voltage raises the overvoltage stress on insulation components such as insulators and surge arresters, requiring focused attention on insulation coordination. Moreover, the larger reignition peak transient current generates stronger electromagnetic interference, which may affect wireless communication and track circuits. In high-speed sections, shielding and filtering measures should be given priority.

The traction network voltage at the train's operating location is shown in Figure 13. At the moment of arc ignition, a high-impedance state arc abruptly appears. As the energy balance of the system is instantaneously disrupted, the traction network voltage undergoes

severe oscillations, followed by periodic oscillations corresponding to arc extinction at current zero-crossings and subsequent reignition.

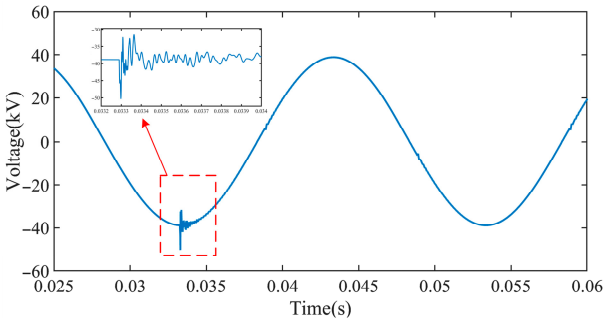


Figure 13. Traction network voltage at a train operating speed of 100 km/h.

The transient currents in the traction power supply system lines at the moment of arc ignition are shown in Figure 14. When the pantograph separates from the catenary, the current path between them is interrupted. At this point, the circuit of the traction power supply system abruptly changes from a closed state to an open state. Subsequently, when the voltage across the pantograph–catenary gap exceeds the breakdown voltage of the gap, the gap breaks down and an arc is generated. This sudden change in the circuit state causes an instantaneous variation in the current, thereby inducing current oscillation. To facilitate a direct comparison, all subfigures in Figure 14 share the same time axis range and the same tick spacing. The waveforms exhibit distinct oscillatory characteristics depending on the conductor. Specifically, the current in the contact wire shows a dominant oscillation frequency of approximately 149.63 kHz, with a duration of about 72 μs; the current in the positive feeder shows a dominant oscillation frequency of approximately 143.83 kHz, with a duration of about 72 μs; the current in the protective wire shows a dominant oscillation frequency of approximately 49.73 kHz, with a duration of about 576 μs; the current in the ground wire shows a dominant oscillation frequency of approximately 54.35 kHz, with a duration of about 576 μs; and the current in the rail shows a dominant oscillation frequency of approximately 143.83 kHz, with a duration of about 72 μs. The spectral content of the traction power supply system lines is concentrated mainly around 0–200 kHz. The differences in oscillation frequency and duration among the conductors are primarily determined by the line parameters and the coupling mechanisms between the conductors. These observations are essential for understanding how transient energy is distributed across the traction network during pantograph–catenary arcing events.

By varying the train operating speed within the range of 20 km/h to 350 km/h, the simulated amplitudes of the conduction current oscillations in each line of the traction power supply system at the moment of arc ignition are presented in Table 9. As the speed of the train increases from 20 km/h to 350 km/h, the peak transient current in the contact wire decreases slightly by 9.38%, and that in the positive feeder decreases by 5.91%. The current in the protective wire shows a slight reduction of 0.81%, while the rail current decreases by 6.96%. In contrast, the ground wire current increases by 2.66%. The traction system is fed by autotransformers (ATs) with fully parallel uplink and downlink lines. The currents listed correspond only to the conductors of the single line on which the train is running. Because the uplink and downlink are electrically connected via ATs, part of the transient current returns through the downlink conductors. Therefore, the sum of the currents on the uplink conductors alone is not zero. The value in the table is the peak amplitude of the oscillatory current waveform in the time domain, whose spectral energy is distributed within 20 MHz.

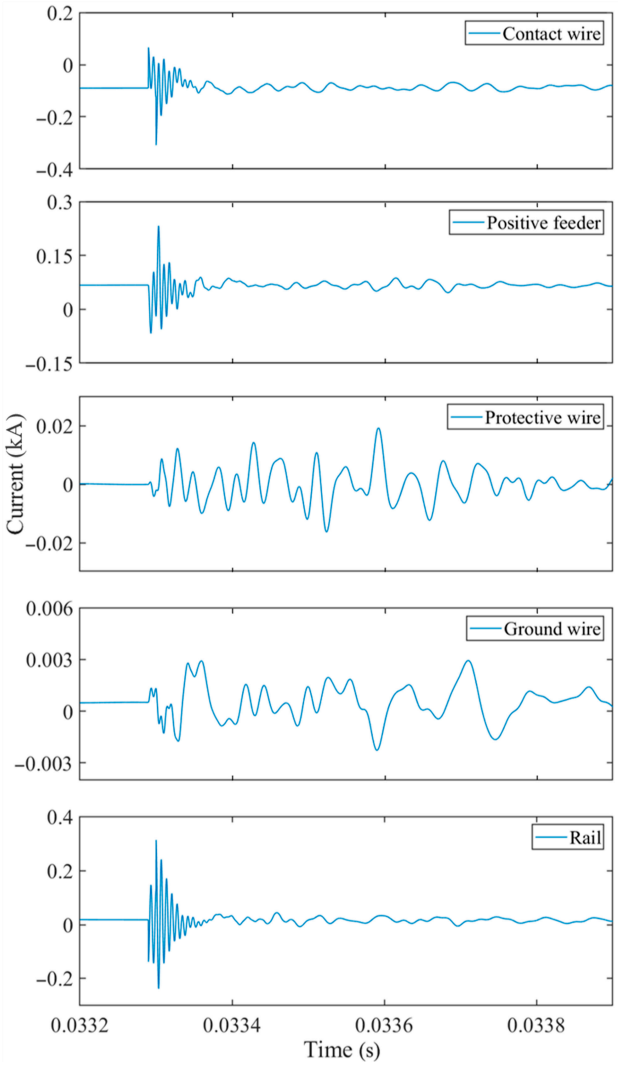


Figure 14. Traction power supply line current at arc initiation when train operates at 100 km/h.

Table 9. Oscillation amplitude of conducted current in each line of the traction power supply system at different speeds.

Speed (km/h)	Contact Wire (A)	Positive Feeder (A)	Protective Wire (A)	Ground Wire (A)	Rail (A)
20	223.055	166.732	19.246	2.441	299.025
60	220.643	165.935	19.234	2.446	297.076
80	220.044	165.495	19.225	2.447	296.032
100	218.949	165.028	19.220	2.451	294.945
120	217.817	164.533	19.210	2.454	293.814
160	215.416	163.460	19.194	2.461	291.430
200	212.857	162.277	19.176	2.469	288.892
250	209.469	160.645	19.151	2.480	285.519
300	205.876	158.846	19.122	2.492	281.948
350	202.104	156.884	19.090	2.506	278.204

When the traction current is the same, a higher train operating speed results in a stronger cooling effect of the airflow on the pantograph–catenary system and the arc. The lower arc energy causes less disturbance to the current of the traction power supply system. Meanwhile, as the train speed increases, the separation distance between the pantograph and catenary during disconnection becomes larger, and the rate of decrease in arc resistance at the moment of arc initiation slows down. Consequently, the oscillation amplitudes of

currents on the contact wire, feeder, protective wire, and rails within the traction power supply system decrease with increasing train operating speed. However, a higher train operating speed generates higher-frequency current components. This alters the impedance distribution of the system, potentially making the loop between the ground wire and the ground a more favorable low-impedance path for high frequencies, thereby diverting a larger proportion of the current. As a result, the oscillation amplitude of the current on the ground wire marginally increases with rising train operating speed.

From an engineering perspective, although the total arc energy decreases with increasing speed, the ground wire experiences higher peak currents due to the increased high-frequency components. Therefore, the grounding system, especially the ground wire itself and its connection points, must be designed for high-speed operating conditions. This implies that a larger cross-section or low-inductance paths may be required. Meanwhile, shielding and filtering of signal cables should be enhanced in high-speed sections to suppress electromagnetic interference. The decrease in peak currents on the main paths including the contact wire, feeder, protective wire, and rail is beneficial for reducing their transient thermal stress. However, because the reduction is limited, it should not be used to justify reducing the current-carrying capacity of these conductors.

To evaluate how the distance between the traction substation and the train affects the transient current distribution, additional simulations were performed at distances of 6 km, 10 km, and 15 km, while keeping all other parameters unchanged. When train operating speed is 20 km/h, the simulation results are summarized in Table 10. As the distance increases from 3 km to 15 km, the peak transient current in the contact wire decreases slightly by 0.36%, and that in the positive feeder decreases by 0.35%. The current in the protective wire shows a substantial reduction of 38.47%, while the rail current decreases by only 0.36%. In contrast, the ground wire current increases by 21.71%. The longitudinal impedance of the contact wire and feeder wire accounts for only a small portion of the total loop impedance. Therefore, the additional impedance caused by an increase in the distance between the arcing location and the traction substation has a negligible effect, and the peak current decreases only slightly. Similarly, the rail serves as the main return path with low impedance and maintains a stable current sharing ratio. Its current remains essentially unchanged, decreasing only marginally. The protective wire carries part of the return current from the arcing location back to the substation, and it has a relatively high impedance per unit length. As the distance between the arcing location and the traction substation increases, the total longitudinal impedance of the protective wire increases significantly, leading to a sharp attenuation of the transient current injected into it. After the current in the protective wire drops, the remaining return current is redistributed through parallel paths. The ground wire, due to its multi-point grounding along the line, carries a very small portion of the transferred current, so its peak current rises slightly.

Table 10. Oscillation amplitude of conducted current in each line of the traction power supply system at different distances between the traction substation and the train.

Distance (km)	Contact Wire (A)	Positive Feeder (A)	Protective Wire (A)	Ground Wire (A)	Rail (A)
3	223.055	166.732	19.246	2.441	299.025
6	222.831	166.605	12.432	2.676	298.655
10	222.567	166.424	11.862	2.852	298.392
15	222.242	166.154	11.842	2.971	297.944

From an engineering perspective, the worst-case stress for the protective wire occurs at the shortest distance, where its peak current is highest. This should be taken as the design basis for protective-wire thermal and electromagnetic withstand. Conversely, the ground

wire experiences its highest peak current at the maximum distance, so grounding system design should consider the far end as a critical location. The near insensitivity of contact wire, feeder, and rail currents to distance means that the arc energy and overvoltage risk are approximately uniform along the line, simplifying protection coordination.

In addition to the distance sensitivity analysis described above, the train speed is also varied from 20 km/h to 350 km/h at a distance of 15 km. The simulation results in Table 11 show that the variation trends of the transient currents in all conductors with increasing train speed are consistent with those observed at the baseline distance of 3 km. Specifically, the peak currents in the contact wire, positive feeder, protective wire, and rail decrease as the speed increases, while the ground wire current increases. This consistency confirms that the influence of train speed on transient current distribution is not qualitatively altered by the distance to the substation, and the conclusions drawn from the 3 km case remain valid for the distance of 15 km.

Table 11. Oscillation amplitude of the conducted current in each line at different speeds when the distance between the arc and the traction substation is 15 km.

Speed (km/h)	Contact Wire (A)	Positive Feeder (A)	Protective Wire (A)	Ground Wire (A)	Rail (A)
20	222.242	166.154	11.842	2.971	297.944
120	216.997	163.954	11.828	2.988	292.732
220	210.710	161.064	11.782	3.271	286.484
350	201.287	156.299	11.702	3.314	277.119

5. Conclusions

This paper establishes an integrated simulation model that combines the traction network with the arc model. The traction network is represented as a multi-conductor transmission line chain circuit including contact wire, positive feeder, protective wire, rail, and ground wire. The arc is modeled using a modified Habedank model, in which the constants P_0 and E_0 are replaced by speed-dependent expressions derived from experimentally validated relationships. Using this model, the transient behavior during pantograph–catenary offline events is systematically analyzed for train speeds from 20 km/h to 350 km/h and for distances to the substation of 3 km, 6 km, 10 km, and 15 km. The results of the study indicate that:

(1) As speed increases, the airflow blowing effect reduces arc energy, leading to a decrease in the peak currents flowing through main pathways such as the contact wire, feeder, protective wire, and rails during arc ignition. However, due to the increased high-frequency components of the current generated at higher speeds, the current shunt on the ground wire increases, causing its peak value to rise instead. Therefore, the grounding system, especially the ground wire itself and its connection points, must be designed for high-speed operating conditions. This implies that a larger cross-section or low-inductance paths may be required. Meanwhile, shielding and filtering of signal cables should be enhanced in high-speed sections to suppress electromagnetic interference.

(2) The increase in speed also alters the intrinsic characteristics of the arc. The rapid elongation of the arc column increases its equivalent resistance and energy requirements, resulting in a higher maximum voltage at arc ignition, a higher steady-state arc voltage, a prolonged extinction time at current zero-crossings, and an increased peak transient current during reignition. The higher reignition peak current and longer arc duration accelerate material wear on both the contact wire and the pantograph strip; therefore, high-speed lines should shorten the pantograph maintenance interval and enhance wear monitoring. The increase in arc voltage raises the overvoltage stress on insulation components such as insulators and surge arresters, requiring focused attention on insulation coordination.

(3) At a constant speed, as the distance between the arcing location and the traction substation increases, the peak transient currents on the contact wire, positive feeder, protective wire, and rail all decrease, while the peak transient current on the ground wire increases. Therefore, the ground wire experiences its highest peak current at the maximum distance, so grounding system design should consider the far end as a critical location.

Author Contributions: Conceptualization, C.L. and J.G.; methodology, C.L., W.X. and J.G.; software, W.X.; validation, C.L., W.X. and X.W.; formal analysis, C.L. and W.X.; data curation, X.W.; writing—original draft preparation, C.L. and W.X.; writing—review and editing, J.G.; visualization, X.W.; supervision, J.G.; project administration, C.L. and X.W.; funding acquisition, J.G. All authors have read and agreed to the published version of the manuscript.

Funding: This research received no external funding.

Data Availability Statement: The original contributions presented in this study are included in the article. Further inquiries can be directed to the corresponding author.

Conflicts of Interest: The authors declare no conflicts of interest.

References

1. Yang, Z.; Xu, P.; Wei, W.; Gao, G.; Zhou, N.; Wu, G. Influence of the Crosswind on the Pantograph Arcing Dynamics. *IEEE Trans. Plasma Sci.* **2020**, *48*, 2822–2830. [CrossRef]
2. Quan, W.; Xu, X.; Liu, X.; Wang, X.; Gao, S. ArcSE: A Dual-Branch Semantic Segmentation Model for Robust Pantograph–Catenary Arcing Detection in Complex Environments. *IEEE Trans. Instrum. Meas.* **2025**, *74*, 2502814. [CrossRef]
3. Song, Y.; Lu, X.; Yin, Y.; Liu, Y.; Liu, Z. Optimization of Railway Pantograph-Catenary Systems for Over 350 km/h Based on an Experimentally Validated Model. *IEEE Trans. Ind. Inform.* **2024**, *20*, 7654–7664. [CrossRef]
4. Song, Y.; Duan, F.; Liu, Z. Analysis of Critical Speed for High-Speed Railway Pantograph-Catenary System. *IEEE Trans. Veh. Technol.* **2022**, *71*, 3547–3555. [CrossRef]
5. Sunar, Ö. Thermal Modeling of Temperature Gradients in Railway Contact Wires During Arcing Process. *IEEE Trans. Power Deliv.* **2024**, *39*, 93–100. [CrossRef]
6. Guo, F.; Gu, X.; Wang, Z.; Wang, Y.; Wang, X. Simulation on Current Density Distribution of Current-Carrying Friction Pair Used in Pantograph-Catenary System. *IEEE Access* **2020**, *8*, 25770–25776. [CrossRef]
7. Huang, K.; Su, D. Extended Pantograph–Catenary Arc Modeling and an Analysis of the Vehicular-Grounding Electromagnetic Transients of Electric Multiple Units. *Energies* **2024**, *17*, 1512. [CrossRef]
8. Niu, D.; Zhu, F.; Qiu, R.; Li, X. Study on the characteristics of off-line arc's radio-frequency and low-frequency electromagnetic exposure inside the high speed rail train. *High Volt. Eng.* **2016**, *42*, 2587–2595. [CrossRef]
9. Yang, Y.; Cao, H.; Zhang, M.; Su, Z.; Hu, M.; Jin, M.; Liu, S. Research on the Influence of Pantograph Catenary Contact Loss Arcs and Zero-Crossing Stage on Electromagnetic Disturbance in High-Speed Railway. *Energies* **2024**, *17*, 138. [CrossRef]
10. Wu, G.; Gu, Z.; Gao, G.; Hao, J.; Zhu, G. Experimental Research on Morphological Characteristics of Pantograph-catenary Arc. *High Volt. Eng.* **2015**, *41*, 3531–3537. [CrossRef]
11. Zou, D.; Xia, Z.; Xu, G.; Sarkar, S.; Atul, J.K.; Shi, G.; Wang, M. Influence of Low Air Pressure on Pantograph–Catenary Arc Model. *IEEE Trans. Plasma Sci.* **2025**, *53*, 1292–1298. [CrossRef]
12. Xu, Z.; Gao, G.; Wei, W.; Yang, Z.; Xie, W.; Dong, K.; Ma, Y.; Yang, Y.; Wu, G. Characteristics of pantograph-catenary arc under low air pressure and strong airflow. *High Volt.* **2022**, *7*, 369–381. [CrossRef]
13. Ma, Y.; Gao, G.; Zhu, G. Numerical Simulation and Analysis of Temperature Distribution of Pantograph-catenary Arc Characteristics of High-speed Train. *High Volt. Eng.* **2015**, *41*, 3597–3603. [CrossRef]
14. Midya, S.; Bormann, D.; Larsson, A.; Schutte, T.; Thottappillil, R. Understanding pantograph arcing in electrified railways—Influence of various parameters. In Proceedings of the 2008 IEEE International Symposium on Electromagnetic Compatibility, Detroit, MI, USA, 18–22 August 2008; pp. 1–6. [CrossRef]
15. Midya, S.; Bormann, D.; Schutte, T.; Thottappillil, R. Pantograph Arcing in Electrified Railways—Mechanism and Influence of Various Parameters—Part II: With AC Traction Power Supply. *IEEE Trans. Power Deliv.* **2009**, *24*, 1940–1950. [CrossRef]
16. Midya, S.; Bormann, D.; Schutte, T.; Thottappillil, R. DC component from pantograph arcing in AC traction system—Influencing parameters, impact, and mitigation techniques. *IEEE Trans. Electromagn. Compat.* **2011**, *53*, 18–27. [CrossRef]
17. Chen, X.; Cao, B.; Liu, Y.; Gao, G.; Wu, G. Dynamic Model of Pantograph-catenary Arc of Train in High Speed Airflow Field. *High Volt. Eng.* **2016**, *42*, 3593–3600. [CrossRef]

18. Zhou, C.; Chen, S.; Qian, P.; Dong, K.; Yang, Z.; Gao, G. Research on the Magnetic Blowing of Lowering Pantograph Arc Extinguishing Under Low Air Pressure. In *2023 Panda Forum on Power and Energy (Panda FPE)*; IEEE: New York, NY, USA, 2023; pp. 1585–1589. [CrossRef]
19. Jin, M.; Hu, M.; Li, H.; Yang, Y.; Liu, W.; Fang, Q.; Liu, S. Experimental Study on the Transient Disturbance Characteristics and Influence Factors of Pantograph–Catenary Discharge. *Energies* **2022**, *15*, 5959. [CrossRef]
20. Xiang, K.; Chen, J.; Xun, J. Simulation study of bow net arc considering air convection heat transfer. *J. Guangxi Univ. Nat. Sci. Ed.* **2023**, *48*, 1134–1146. [CrossRef]
21. Liang, J.; Shi, L.; Wang, F.; Zhao, Y.; Liu, Y.; Li, M.; Li, X. Safety assessment of electromagnetic exposure to arcing in electrified railway bow networks. *IEEE Access* **2024**, *12*, 143352–143377. [CrossRef]
22. Zhang, J.; Yang, J.; Liu, Y.; Guan, J.; Xu, K.; Zhang, K. Study on the Transient Response Law of Pantograph-catenary at the Positioning Point of High-speed Railway Catenary. *J. Railw. Eng. Soc.* **2025**, *42*, 70–75. [CrossRef]
23. Ma, Y.; Liu, Z.; Wen, Y.; Ma, L.; Zhang, J. Effect of vehicle speed on pantograph arc discharge for high speed EMU. *J. Beijing Jiaotong Univ.* **2013**, *37*, 99–103. [CrossRef]
24. Pan, L.; Xie, B.; Chen, L.; Xing, T.; Zhang, H.; Lu, Y.; Song, Y. Study on the Influencing Factors of Electrical Characteristics of Articulated Split-Zone Insulator Arc. *Energies* **2024**, *17*, 3883. [CrossRef]
25. Bosyi, D.; Antonov, A.; Zemskyi, D.; Barresi, M.; Mazorchuk, V. Power Quality at Railway Traction Substations in Ukraine and Its Role in Power System Stability. In Proceedings of the 2025 International Conference on Clean Electrical Power (ICCEP), Villasimius, Italy, 24–26 June 2025; pp. 735–740. [CrossRef]
26. Yang, H.; Du, X.; Chen, B.; Cao, Y.; Zheng, L.; Wang, H. The Influence of Electrified Railway Traction Power Supply System on the Power Quality of Regional Power Grid. In Proceedings of the 2023 IEEE International Conference on Sensors, Electronics and Computer Engineering (ICSECE), Jinzhou, China, 18–20 August 2023; pp. 13–18. [CrossRef]
27. Kar, P.; Pradhan, P.; Das, B.; Bhalja, B. Power Flow Analysis of 2 × 27.5 kV Traction Network with Single-Phase Transformer and V/V Transformer at Traction Substation. In Proceedings of the 2024 Third International Conference on Power, Control and Computing Technologies (ICPC2T), Raipur, India, 18–20 January 2024; pp. 118–123. [CrossRef]
28. Wang, H.; Liu, W.; Li, Q.; Ma, Q.; Liu, T. Dynamic Power Flow Calculation of AC Electrified Railway Based on Source-grid-load Unified Chain Circuit. *Proc. CSEE* **2022**, *42*, 3936–3953. [CrossRef]
29. Carson, J.R. Wave Propagation in Overhead Wires with Ground Return. *Bell Syst. Tech. J.* **1926**, *5*, 539–554. [CrossRef]
30. Wu, G.; Qian, P.; Liu, W.; Gao, G.; Li, H. Research progress of high-speed railway pantograph arc: Influencing factors and prevention methods. *Acta Phys. Sin.* **2025**, *74*, 8–28. [CrossRef]
31. Wang, Z.; Li, Z.; Han, C.; Guo, F. Mathematical Model of Pantograph Arc Based on Probability Distribution of Arc Parameters. *IEEE Trans. Transp. Electrif.* **2023**, *9*, 2026–2037. [CrossRef]
32. Tang, Y.; Zhu, F.; Chen, Y. Research on the Influence of Train Speed Change on the EMI of Pantograph-Catenary Arc to Main Navigation Stations. *Appl. Comput. Electromagn. Soc. J.* **2021**, *36*, 450–457. [CrossRef]

Disclaimer/Publisher's Note: The statements, opinions and data contained in all publications are solely those of the individual author(s) and contributor(s) and not of MDPI and/or the editor(s). MDPI and/or the editor(s) disclaim responsibility for any injury to people or property resulting from any ideas, methods, instructions or products referred to in the content.